International Journal of Heat and Mass Transfer 99 (2016) 268–282

Contents lists available at ScienceDirect

International Journal of Heat and Mass Transfer

journal homepage: www.elsevier.com/locate/ijhmt

Numerical study on characteristics of heat transfer and friction factor in a circular tube with central slant rods

Peng Liu, Nianben Zheng, Feng Shan, Zhichun Liu, Wei Liu *

School of Energy and Power Engineering, Huazhong University of Science and Technology, Wuhan 430074, China

ARTICLE INFO

Article history:
Received 21 November 2015
Received in revised form 1 March 2016
Accepted 15 March 2016
Available online 16 April 2016

Keywords:
Central slant rod
Heat transfer enhancement
Laminar flow
Physical quantity synergy principle
Multi-vortex structure

ABSTRACT

In the present work, a numerical study on the characteristics of heat transfer and friction factor of laminar water flow in a circular tube fitted with a new tube insert (central slant rod inserts) is presented. Results reveal that the new inserts can fully disturb the core flow in the tube and create multiple longitudinal vortex structures, which are confirmed to be excellent flow structures for heat transfer enhancement. In addition, we carried out stereoscopic particle image velocimetry (SPIV) measurements in exactly the same facility as that of the numerical study to validate the accuracy of our numerical study. The results show good agreement between the experiment and numerical simulation. Following this, the effects of three parameters of central slant rods, including the slant angle, pitch and length in the radial direction, are discussed numerically. The computational results indicate that a moderate slant angle ranging from 20° to 30° can obtain the largest Nusselt number; however, the effect of slant angle on the friction factor is quite limited. The Nusselt number and friction factor both increase with a decrease in rod pitch and an increase in rod length in the radial direction. The simulation results show that the Nusselt number and friction factor are enhanced by 1.81–5.05 times and 2.49–6.92 times, respectively, to that of a plain tube. The performance ratio $R3$ values are in the range of 1.74–4.60. Empirical formulas for Nu and f are obtained based on calculation results. All results indicate that the central slant rod is a promising high-performance tube insert for heat transfer enhancement in practical applications.

1. Introduction

Heat exchangers are widely used in industrial fields such as power generation, chemical industry, aviation, aerospace, electronics, metallurgy, medicine, and materials. Considering the current energy crisis, it is significant to intensify the heat transfer process of heat exchangers in order to save energy. Numerous heat transfer augmentation techniques have been proposed by scientists and researchers around the world [1]. These techniques are generally divided into two categories: passive techniques (requiring no external power) and active techniques (requiring external power).

For the tube side heat transfer in shell-and-tube heat exchangers, passive techniques including surface coating, wave surfaces, rough and extended surfaces, convoluted (twisted) tube and tube inserts (turbulators and vortex generators) are more widely used because no external power is required. As a significant group of enhancement techniques, various tube inserts have been researched and proposed for heat transfer enhancement. Among them, the twisted tape technique has been widely used to produce compact heat exchangers due to its low cost and ease of manufacture and installation. Manglik and Bergles et al. [2,3] conducted experimental investigations of heat transfer and pressure drop in a tube fitted with inserts of twisted tape under laminar and turbulent flow conditions. Their results show that the twisted tape could induce turbulence and vortex motion (swirl flow) which led to a thinner boundary layer and consequently the generation of a higher heat transfer coefficient. On the other hand, the swirl flow induced by the twisted tape cause an increase in flow resistance which resulted in performance factor, at an equivalent pumping power, less than unity. In order to improve the thermal–hydraulic performance, various attempts have been made to modify the twisted tape technique. Some of them aimed to reduce the friction loss [4–7]: Saha et al. [4] presented the characteristics of friction and heat transfer for laminar flow in a circular tube fitted with regularly spaced twisted-tape elements; Jaisankar et al. [5] investigated the characteristics of friction and heat transfer for twist fitted with rod and spacer inserts in a tube; Krishna et al. [6] studied the heat transfer and pressure drop of a circular tube fitted with a straight full twisted tape. Results of these studies all indicate that the friction factor is observably reduced along with slight decrease in heat transfer compared to the corresponding value of traditional

* Corresponding author.
E-mail address: w_liu@hust.edu.cn (W. Liu).

http://dx.doi.org/10.1016/j.ijheatmasstransfer.2016.03.059
0017-9310/

Nomenclature

l	the length of rod in the radial direction, mm
p	the pitch of rod, mm
q	heat transfer rate per unit area, W/m^2
D	inner diameter of the tube, mm
L	the full length of tube, mm
T	temperature of water, K
T_c	temperature at the center position of inlet cross-section, K
u	flow velocity, m/s
u_c	velocity at the center position of inlet cross-section, m/s
R	inner radius of the tube, mm
r	the distance between the fluid particle and the center of the tube, mm
c_p	specific heat at constant pressure of water, J/kg K
Re	Reynolds number
Nu	Nusselt number
f	friction factor
u_i	the velocity component in the three-dimensional space, m/s
h	heat transfer coefficient, W/m^2 K
P	pressure of water, Pa
T_w	temperature on the tube wall, K
T_m	fluid bulk temperature inside tube, K
$R3$	comprehensive heat transfer performance coefficient
Nu_0	Nusselt number of a plain tube
f_0	friction factor of a plain tube
S	non-dimensional slant angle

Greek symbols

θ	the slant angle of rod, °
ρ	density of water, kg/m^3
μ	dynamic viscosity of water, kg/m s
λ	thermal conductivity of water, W/m K
β	synergy angle, °
θ_1	synergy angle, °

twisted tape, and consequently the thermal–hydraulic performance is improved. Other researchers aimed to further enhance the heat transfer on the basis of typical twisted tapes [8–11]: Tarasevich et al. [8] proposed twisted tapes with wire-wound or wire-laced ribs on its surface to enhance the heat transfer; Eiamsa-Ard et al. [9] experimentally studied the performance assessment in a tube with alternate clockwise and counter-clockwise twisted-tape inserts; Murugesan et al. [10] and Chang et al. [11] investigated the inserts of V-cut twisted tape and broken twisted tape, respectively. They found that these modifications on twisted tape inserts can give assurance for the enhancement of both the heat transfer rate and the thermal enhancement factor.

In addition, various other forms of tube inserts have been proposed [12–19]. Martínez et al. [12] experimentally studied the heat transfer of laminar and transitional Newtonian and non-Newtonian flows in tubes with wire coil inserts. The results indicated that the wire coil inserts could enhance heat transfer when the Reynolds number is larger than 500, and the maximum Nusselt number augmentations of 7.5 at Re = 1900 is achievable. Fan et al. [13] numerically investigated turbulent heat transfer and flow characteristics in a circular tube fitted with louvered strip inserts. It was found that the louvered strip insert has a fairly good overall thermo-hydraulic performance with the *PEC* value lying in the range of 1.60–2.05. Jasiński [14] proposed a ball turbulent inserts fitted in a circular tube and numerically investigated the effects of diameter ratio and longitudinal distance ratio on the thermo-hydraulic performance of turbulent flow. The results show that the Nusselt number increases with an increase in diameter ratio, and the Nusselt number increases initially and then it begins to decrease with an increase in longitudinal distance ratio. Zhang et al. [15] studied numerical characteristics of the heat transfer and friction factor in a tube fitted with helical screw-tape without core-rod inserts. It was found that thees inserts could obtain a good overall heat transfer performance with an *PEC* value of between 1.58 and 2.35 when *Re* number ranges from 4000 to 20,000. Deshmukh et al. [16] developed a vortex generator in a circular tube and investigated its heat transfer characteristics and the friction factor for turbulent flow. It was found that this vortex generator could effectively strengthen the heat transfer with Nusselt numbers of approximately 150–500% higher than the corresponding values of a smooth tube. Zhang et al. [17] numerically studied heat transfer and flow characteristics of a tube fitted with a double spiral spring. They found that the double spiral spring inserts could obtain augmentation of 0.74–1.78 times for heat transfer and 2.83–8.79 times for friction factor when compared to a plain tube, and the *PEC* value could reach 1.5. Tu et al. [18,19] developed a small pipe insert which can guide the core flow through the small pipe to the boundary layer. It was found that the small pipe insert has an excellent overall thermo-hydraulic performance both in laminar and turbulent tube flow. The majority of these can produce swirl flow in the tube which causes better fluid mixing and consequently results in the enhancement of heat transfer.

Based on a survey of the literature, we find that most tube inserts are proposed from experience, and the designs lack theoretical guidance. In theory, tube flow can generally be divided into two parts: boundary flow and core flow [20]. Principles for increasing efficiency of core flow have been proposed by Liu and Yang [21,22]. They suggest that core flow temperature should be made more uniform by increasing the effective thermal conductivity of the fluid and enhancing the fluid mixing and disturbance of the core flow field. Others suggest that fluid shear force should be reduced by minimizing the velocity gradient of the flow, and the

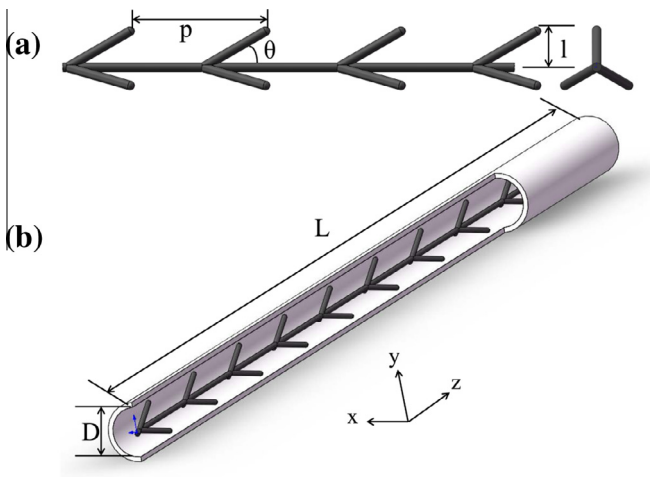

Fig. 1. (a) Geometry of the central slant rod insert, and (b) the circular tube fitted with central slant rod inserts.

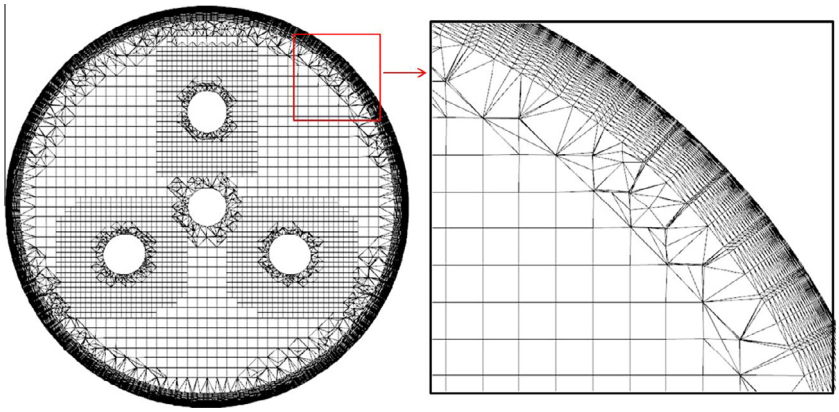

Fig. 2. Grid in the cross-sectional plane at $z = 50$ mm in the tube.

Table 1
Grid independence test.

	Grid number	*Nu*	*f*	*PEC*
Model 1	6,000,000	12.3429	0.7255	1.8825
Model 2	8,500,000	10.7911	0.6891	1.6743
Model 3	11,000,000	10.8415	0.6903	1.6811

disturbance to the boundary flow should be reduced to avoid large momentum loss by breaking the continuous extended surface. Furthermore, to provide guidelines for achieving energy savings and overall thermal performance by improving the balance between heat transfer enhancement and pressure drop, our group has carried out several heat transfer optimization studies [23–27]. The theoretical results all show that a structure of multi-longitudinal swirling flows is the optimized flow field in a circular tube for heat transfer enhancement.

On the basis of previous studies, the contribution of this paper is to propose a new type of tube insert named central slant rod to verify the multi-longitudinal swirling flow structure in a tube for better thermal–hydraulic performance. A numerical study has been carried out to investigate the characteristics of heat transfer and friction factor in a circular tube with inserts of central slant rods. In addition, we will also discuss the effects of three parameters of central slant rods, including the slant angle, pitch and length in the radial direction. Moreover, stereoscopic particle image velocimetry (SPIV) measurements of the flow field for exactly the same setup as that in the numerical study has been conducted to validate the accuracy of our numerical simulation.

2. Numerical modeling and PIV experimental setup

2.1. Physics model

The geometrical model of central slant rod(s) is shown in Fig. 1. The diameter of the slant rods, which are connected by a central rod, is 2 mm. The geometric parameters are as follows: the tube length $L = 500$ mm; inner diameter $D = 20$ mm; the slant angle of rods $\theta = 20°$, 30° or 40°; the pitch of rods $p = 30$, 40, or 50 mm; and the length of rods in the radial direction $l = 7$, 8, or 9 mm. The choosing the central slant rods geometric parameters is based on the experience and reference to the predecessors' research, such as louvered strip inserts [13], small pipe insert [18]. In this study, water is selected as the working fluid and heat conduction in the slant rods and central rod is neglected. The thickness of solid wall is also not considered.

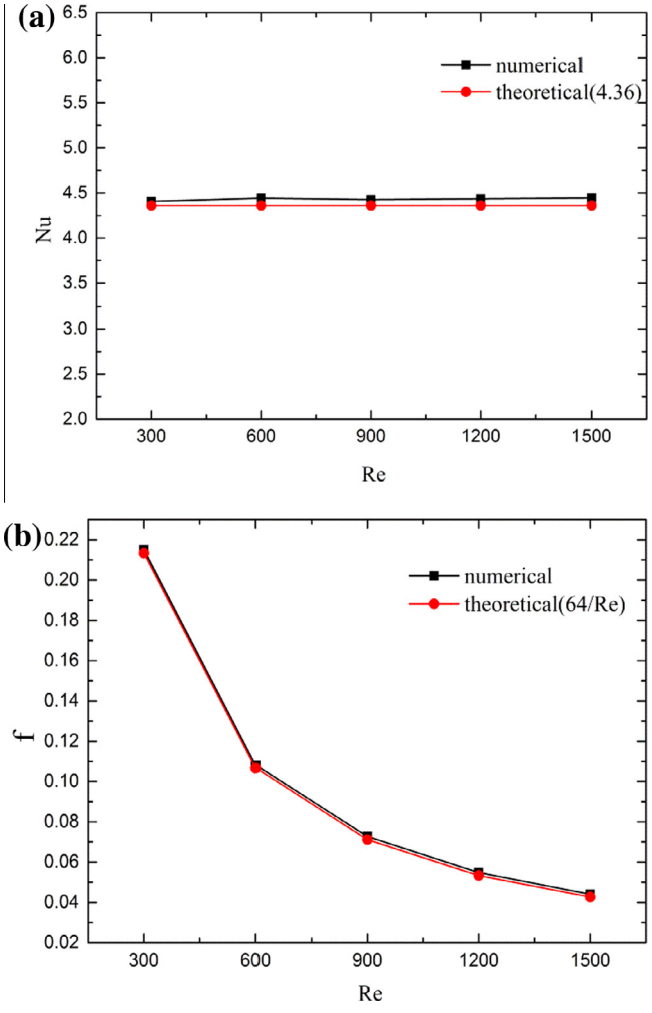

Fig. 3. Comparison of the numerical results and the theoretical values of the Nusselt number (*Nu*) and the friction factor (*f*) of the plain tube: (a) *Nu*, (b) *f*.

2.2. Governing equations

The numerical simulation conditions are assumed to be three-dimensional, laminar and steady. The following assumptions are made for simplifying the calculations: (1) the physical properties of the fluid are constant and are set to be: $\rho = 998.2$ kg/m^3, $\mu = 1.003 \times 10^{-3}$ kg/m s, $c_p = 4182$ J/kg K and $\lambda = 0.6$ W/m K; (2)

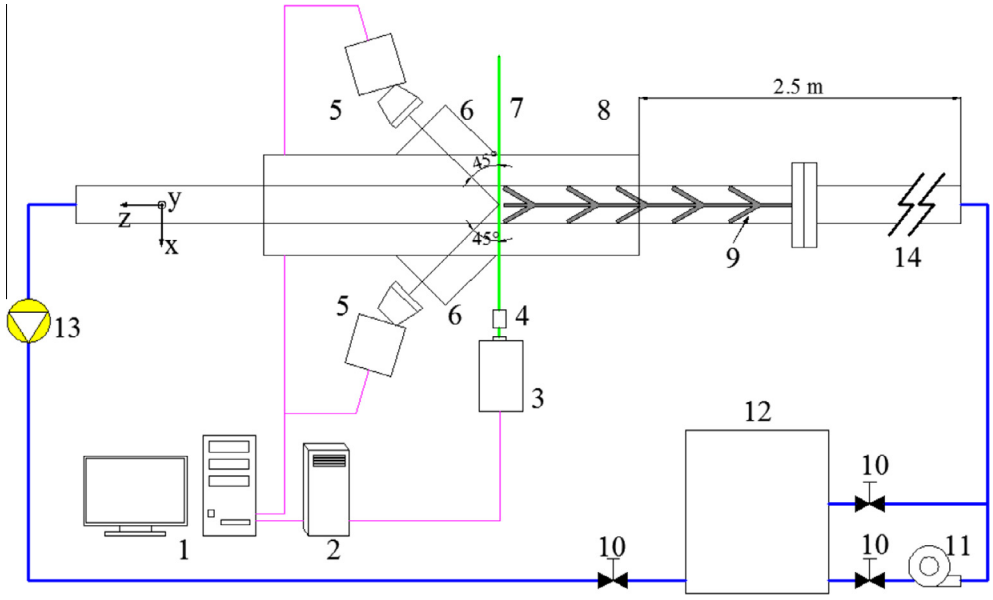

Fig. 4. Schematic of the stereoscopic-PIV system. 1 computer, 2 PIV supply unit, 3 laser, 4 lenses, 5 CCD cameras, 6 water prism, 7 light sheet, 8 test section, 9 centrally slant rod inserts, 10 control valves, 11 water pump, 12 water tank, 13 electromagnetic flowmeter, 14 upstream tube.

Table 2
Overview of the relevant experimental parameters.

Upstream pipe	Diameter	20 m
	Length	2.5 m
	Material	Steel
Test pipe	Diameter	20 mm
	Material	Glass
	Wall thickness	2 mm
Central slant rod inserts	Length	500 mm
	Slant angle θ	30°
	Pitch p	30 mm
	The radial direction l	9 mm
Water pump	Type	Centrifugal pump
Flowmeter	Type	Electromagnetic Flowmeter
Flow	Fluid	Water
	Re	480, 1000, 1750
Seeding	Type	Hollow glass sphere
	Specific weight	1 g/cm^3
	Diameter	12 μm
	Concentration	5 g/m^3
Light sheet	Laser type	Nd:YAG
	Maximum energy	200 mJ/pulse
	Wave length	532 nm
	Pulse duration	6 ns
	Thickness	≈1 mm
Camera	Type	CCD
	Resolution	2048 × 2048 px
	Discretization	12 bit
	Repetition rate	7.5 Hz
	Lens focal length	60 mm
Imaging	f-number	11
	Viewing angles	±45°
	Viewing area	25 × 25 mm
	Exposure time-delay	2.4, 1.9, 1.3 ms
PIV analysis	Reconstruction method	Three-dimensional calibration
	Interrogation area (IA)	32 × 32 px
	Overlap IA	50%

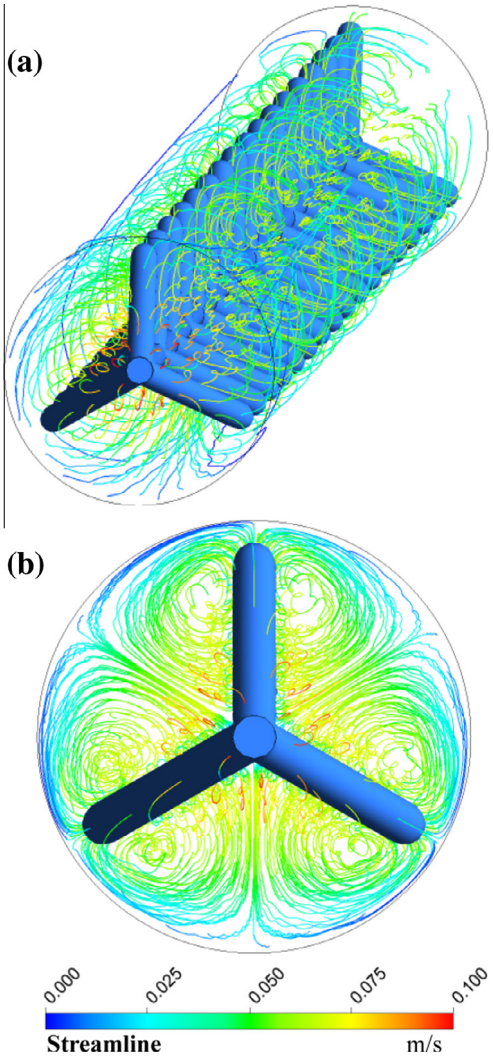

Fig. 5. Streamline of tube with central slant rod inserts at $Re = 900$, $\theta = 30°$, $l = 9$ mm, $p = 30$ mm.

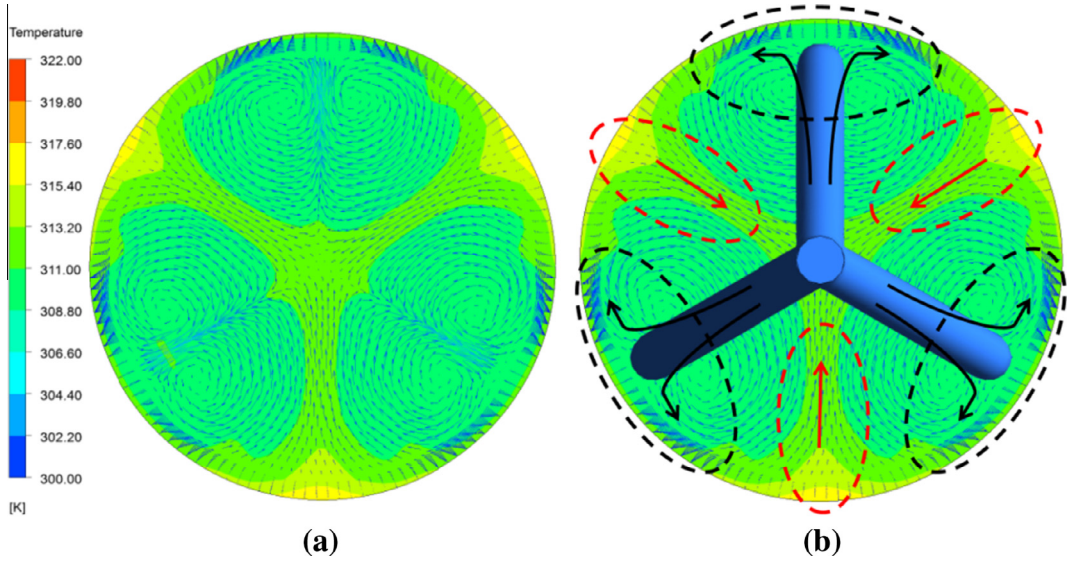

Fig. 6. Temperature contours and transverse velocity components on outlet plane at $Re = 900$, $\theta = 30°$, $l = 9$ mm, $p = 30$ mm. (For interpretation of the references to color in this figure legend, the reader is referred to the web version of this article.)

the fluid is incompressible, isotropic and continuous; (3) the fluid is a Newtonian fluid; and (4) the effect of both thermal radiation and gravity is ignored. Equations of continuity, momentum and energy for fluid flow are given as follows:

$$\text{Continuity equation}: \quad \frac{\partial u_i}{\partial x_i} = 0 \quad (i = 1-3) \tag{1}$$

$$\text{Momentum equation}: \quad \rho u_i \frac{\partial u_j}{\partial x_i} = -\frac{\partial p}{\partial x_i} + \frac{\partial}{\partial x_i}\left(\mu \frac{\partial u_j}{\partial x_i}\right) \quad (j = 1-3) \tag{2}$$

$$\text{Energy equation}: \quad \rho c_p \left(u_i \frac{\partial T}{\partial x_i}\right) = \lambda \left(\frac{\partial^2 T}{\partial x_i^2}\right) \tag{3}$$

2.3. Boundary conditions

A constant heat flux condition is specified for the tube wall. At the tube inlet, fully developed flow and temperature boundary conditions are applied, which are defined as follows:

Inlet temperature condition:

$$T = T_c + \frac{qR}{\lambda}\left[\left(\frac{r}{R}\right)^2 - \frac{1}{4}\left(\frac{r}{R}\right)^4\right] \tag{4}$$

Inlet velocity condition:

$$u = u_c\left(1 - \frac{r^2}{R^2}\right) \tag{5}$$

where T_c and u_c are the temperature and velocity at the center position of the inlet cross-section, respectively.

At the outlet, the outflow condition is used. On the tube walls and the surfaces of the slant rods and central rod, no slip conditions are imposed.

2.4. Computation scheme and validation

The Reynolds number (Re), heat transfer coefficient (h), Nusselt number (Nu), and Fanning friction coefficient (f) are defined as follows:

$$Re = \frac{\rho u D}{\mu} \tag{6}$$

$$h = \frac{q}{T_w - T_m} \tag{7}$$

where T_w is temperature on the tube wall and T_m is fluid bulk temperature inside the tube:

$$T_m = \frac{\int_0^R uTrdr}{\int_0^R urdr} \tag{8}$$

$$Nu = \frac{hD}{\lambda} \tag{9}$$

$$f = \frac{\Delta P}{\left(\frac{1}{2}\rho u^2\right)(L/D)} \tag{10}$$

The performance ratio $R3$ [28] is defined as following ways:

$$(Re_a)^3 f_a = (Re_c)^3 f_c \tag{11}$$

where Re_a – augmented case Reynolds number; Re_c – equivalent Reynolds number of smooth tube at same pressure drop (equal pumping power); f_a – augmented case friction factor; f_c – equivalent smooth tube friction factor.

According the $f_c = 64/Re_c$

$$Re_c = \left((Re_a)^3 f_a / 64\right)^{0.5} \tag{12}$$

This expression gives a value of Reynolds number which is equivalent to smooth tube having same pressure drop as that of produced by the insert. At this equivalent Reynolds number Re_c, calculate the Nu_c value for smooth tube flow. The expression formula of performance ratio $R3$ is defined as:

$$R3 = Nu_a / Nu_c \tag{13}$$

Fig. 2 shows the meshing grid at $z = 50$ mm of the computational model with $\theta = 30°$, $p = 30$ mm and $l = 9$ mm. The grid in the region near the tube wall, which is highly refined, is considered to be the boundary layer. Local grid refinement is also applied to the region near the surfaces of slant rod inserts. For the core space of the circular tube, hexahedral meshes are adopted, while in the transition region tetrahedral meshes are used.

Prior to the numerical simulation, the grid independence was checked by using different of grid cell numbers of 6,000,000, 8,500,000 and 1,100,000. The geometric parameters of the model are as follows: $\theta = 30°$, $l = 9$ mm and $p = 30$ mm, and the numerical

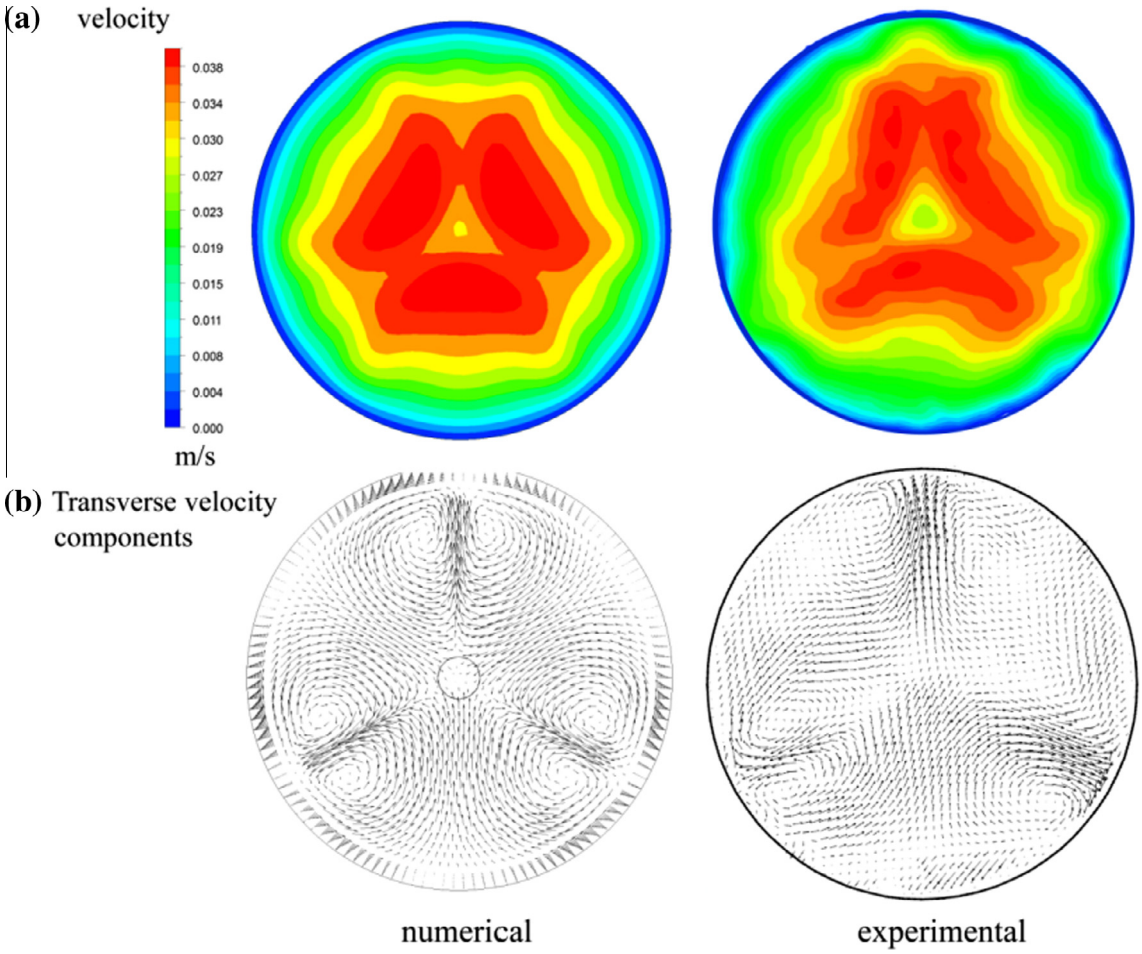

Fig. 7. Comparison between the experimental results and numerical results on same cross-sectional plane at $Re = 480$, $\theta = 30°$, $l = 9$ mm, $p = 30$ mm. (a) velocity contours; (b) transverse velocity components.

simulation is performed at a Reynolds number of 300. The results of the grid independence test are listed in Table 1. The table indicates that the deviation in the results is quite limited when the number of grid cells increases above 8,500,000, and the deviations of *Nu*, *f*, and *PEC* between Model 2 and Model 3 are approximately 0.5%, 0.1% and 0.4%, respectively. Therefore, the grid system of Model 2 with 8,500,000 grid cells is applied to this study.

In this study, the commercial CFD software FLUENT 14.0, based on the finite volume method, is used. The SIMPLE algorithm is used to find a solution for the coupling between the pressure and velocity. The convergence criterion is that the norms of the residuals for the continuity and momentum equations are less than 10^{-6}, while the energy equation's residual is less than 10^{-8}.

To verify the numerical method described above, a comparison is made between the Nusselt number (*Nu*), the friction factor (*f*), and their theoretical values of the plain tube under fully developed laminar flow, as shown in Fig. 3. The deviations between the numerical results and the theoretical values are limited to ±2% for the Nusselt number and ±3.5% for the friction factor, respectively. Therefore, the numerical simulation method has reasonable accuracy.

2.5. Stereo PIV experimental setup

With the stereo-PIV, we can measure all three components of the velocity in the plane of the laser light sheet. The Stereo-PIV system is presented in Fig. 4. The date acquisition is performed with software (TSI Insight 3G) and calculation of the vector field is performed by a commercial PIV-software (Lavision, Davis 8.3.0). In this experiment, we use the size of the interrogation window of 32×32 pixels with a 50% overlap. And the average vector field is calculated from 400. The parameters used for the PIV measurement are presented in Table 2.

3. Results and discussion

3.1. Heat transfer enhancement mechanism of tube with central slant rods

When the tube is inserted with central slant rods, counter-rotating vortices or longitudinal vortex flows are generated. An example of the streamlines at $Re = 900$, $\theta = 30°$, $l = 9$ mm and $p = 30$ mm is shown in Fig. 5. It is clear that the fluid flow has been divided into six main streams due to the confinement of the tube wall and slant rods. In other words, a multi-vortex flow structure in the core flow area of tube is achieved by inserting the slant rods. It is known from the research of Hui et al. [24] that a flow field with multi-vortices in the core area presents excellent performance in heat transfer enhancement. Therefore, it is credible that a tube with central slant rod inserts has gained excellent performance in heat transfer enhancement.

Fig. 6 shows the temperature contours and transverse velocity components on the outlet plane at $Re = 900$, $\theta = 30°$, $l = 9$ mm, and $p = 30$ mm. As shown in Fig. 6(a), six vortices can clearly be

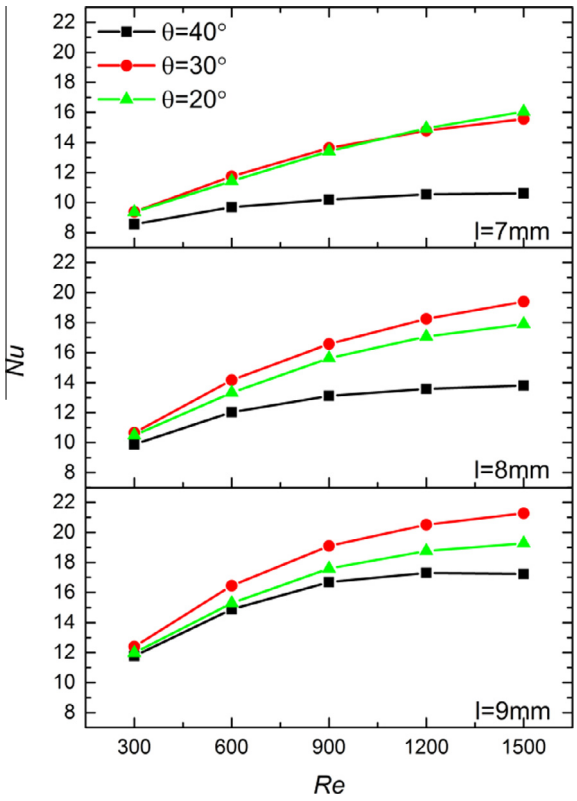

Fig. 8. Variation of the Nusselt number with Reynolds number for different angles at p = 40 mm.

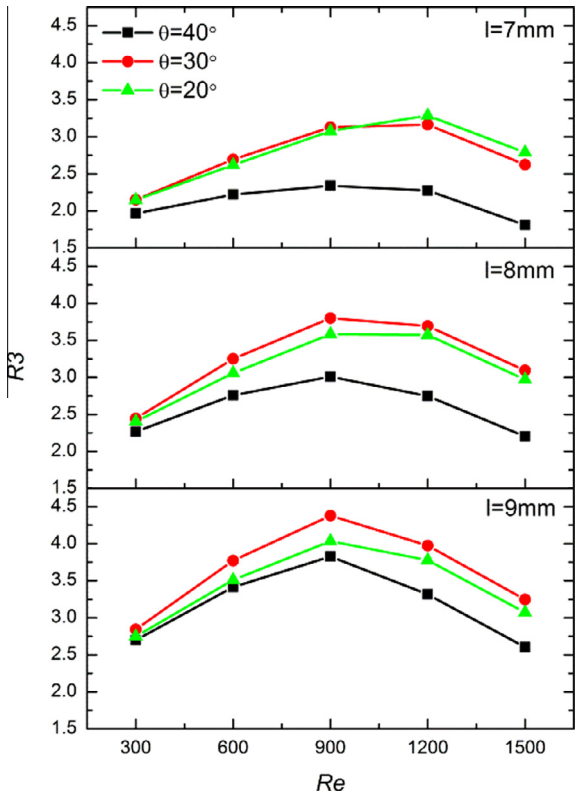

Fig. 10. Variation of the performance ratio $R3$ with Reynolds number for different angles at p = 40 mm.

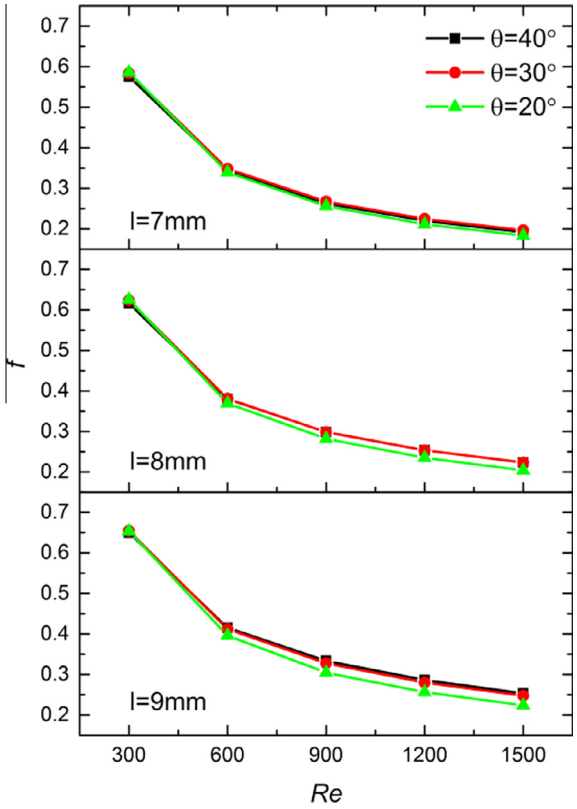

Fig. 9. Variation of the friction factor with Reynolds number for different angles at p = 40 mm.

seen from the transverse velocity components. The heat transfer enhancement mechanism can be analyzed from Fig. 6(b) as follows: as the fluid flows around the slant rod, part of the cold fluid is guided from the core flow region towards the tube wall. It is separated at both sides after impinging on the tube wall. These two fluids then respectively impinge towards the fluid separated by the other slant rod in the regions depicted by red ellipses. This is immediately followed by the higher temperature fluids in these regions being forced to flow towards the core flow region. Therefore, the cold fluid in the core flow region and the heated fluid in the region near the tube wall become fully mixed, and more homogeneous temperature contours in the cross-sectional plane are achieved. According to the researches of Liu et al. [21,22], it is clearly observed that a thin equivalent thermal boundary layer is formed in the tube flow inserted with a central slant rod. This consequently enlarges the temperature gradient of the fluid near the tube wall, and thereby enhances the heat transfer between the fluid and the tube wall.

SPIV (Stereo-Particle image velocimetry) measurements of the flow field at Re = 480, θ = 30°, l = 9 mm and p = 30 mm have been conducted to validate the flow structure obtained by the numerical simulation. A comparison between the experimental and numerical results is presented in Fig. 7. It is seen from Fig. 7(a) that the velocity distribution on the cross-sectional plane of the experimental results correlates well to that of the numerical results, and the maximum deviation is within ±5%. Moreover, three pairs of vortices can be seen at the same regions in the cross-sectional plane of the numerical and experimental results, as shown in Fig. 7(b), and the maximum transverse velocity components in both are approximately 0.01 m/s. Therefore, the flow structure with multi-vortices of the tube with central slant rods has been validated. This shows that the numerical simulation model has reasonable accuracy.

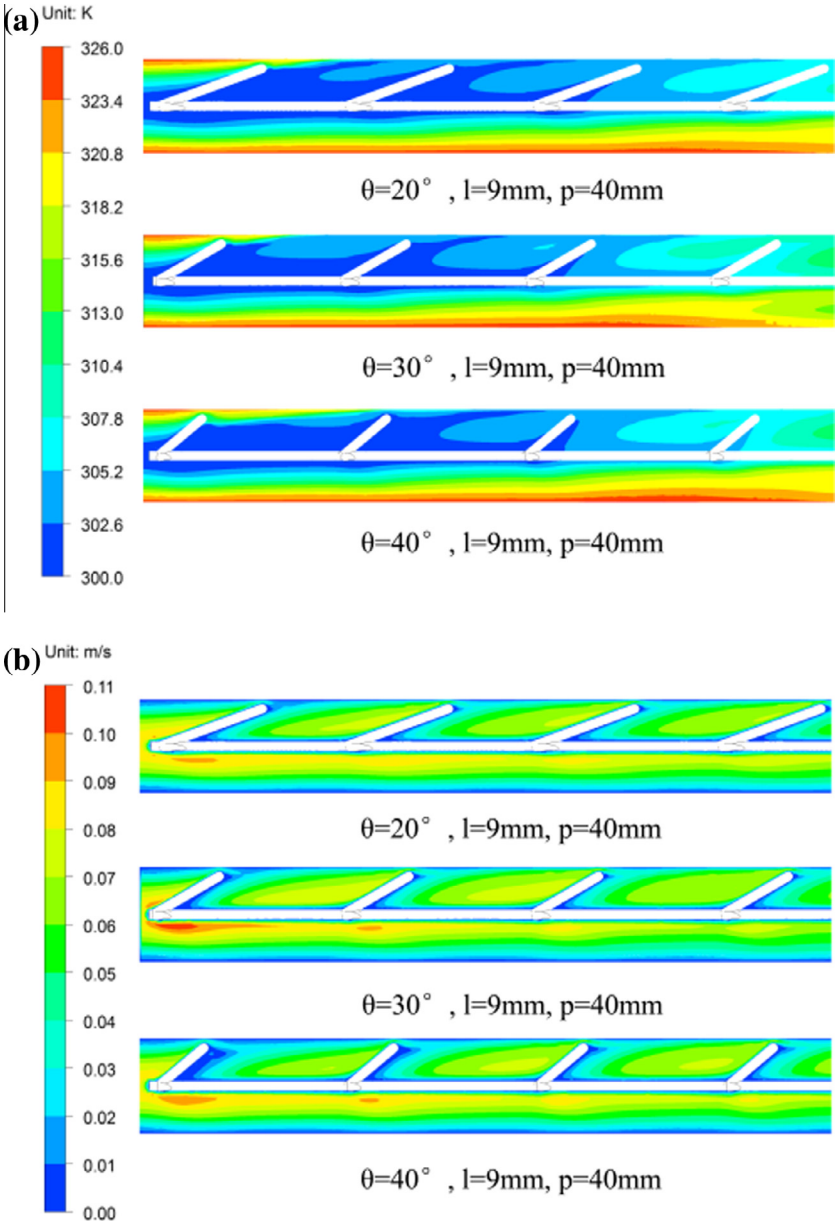

Fig. 11. Temperature contours (a) and velocity contours (b) at Re = 900, p = 40 mm, l = 9 mm.

3.2. Effects of the slant angle θ

The variations in the average Nusselt number, friction factor and performance ratio $R3$ versus the Reynolds number for different slant angles at p = 40 mm are shown in Figs. 8–10. From Fig. 8, it is found that the average Nusselt numbers of tubes with central slant rods all increase with increasing Reynolds number, and they are considerably larger than that of the plain tube (4.36). This verifies that the central slant rod has a positive effect on heat transfer enhancement. Furthermore, when l = 9 mm, the central slant rod with θ = 30° obtains the largest Nu value, while that with θ = 40° obtains the smallest. When l = 8 mm, a similar trend is found, but the difference between θ = 30° and θ = 20° is limited. When l = 7 mm, the Nusselt number of the central slant rod at θ = 20° is almost the same as that at θ = 30°. The Nusselt number initially increases with an increase in the slant angle, and then tends to decrease with a further increase in the slant angle. Moreover, the optimum slant angle for the Nusselt number decreases with a decrease in length of the rod in the radial direction (l), and the optimum slant angle ranges from 20° to 30°. In other words, the shorter the rod length in the radial direction, the smaller the optimum slant angle. The friction factor increases an increase in the slant angle, and the effect of slant angle on the friction factor is enhanced with an increase in rod length in the radial direction, as shown in Fig. 9. In addition, with an increase of Reynolds number, the effect of slant angle on the friction factor increases. However, the effects of slant angle on the friction factor are quite limited. Therefore, the variation of performance ratio $R3$ versus the slant angle has a similar tendency to that of the Nusselt number, as shown in Fig. 10. When l = 7 mm, the performance ratio $R3$ value of θ = 20° and 30° are almost the same at different Reynolds number, and they are both higher than that of θ = 40°. With the increases of l, the performance ratio $R3$ value of θ = 30° is getting more and more high than that of θ = 20°. The results indicate that there is an optimum slant angle for overall thermal performance located between 20° and 30°, and the optimum slant angle

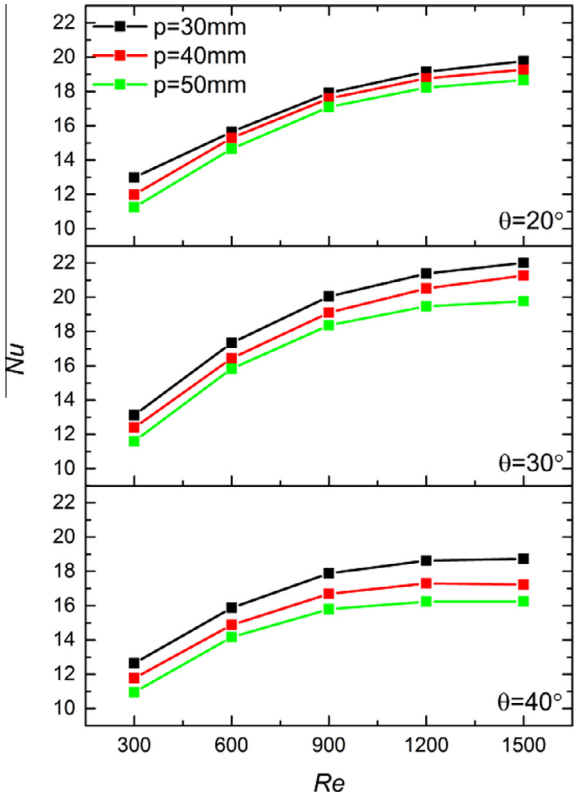

Fig. 12. Effects of the pitch of rod on the average Nusselt number at $l = 9$ mm.

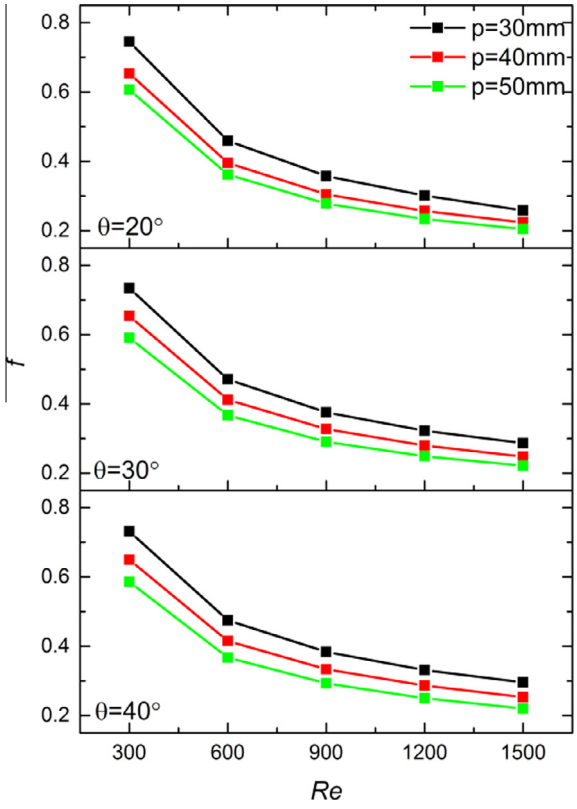

Fig. 13. Effects of the pitch of rod on the friction factor at $l = 9$ mm.

increases with the increase of l. When $p = 30$ and 50 mm, the effects of slant angle on the average Nusselt number, friction factor and performance ratio $R3$ have a similar variation regulation.

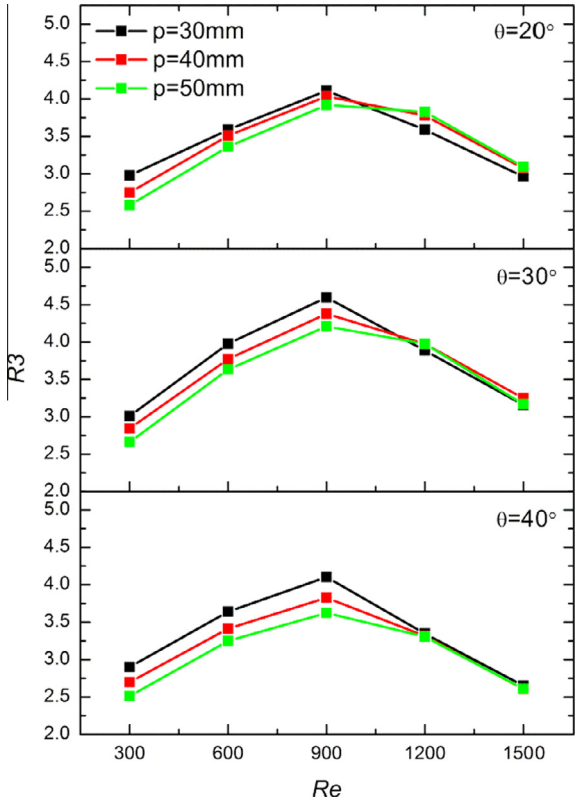

Fig. 14. Effects of the pitch of rod on the performance ratio $R3$ at $l = 9$ mm.

The temperature and velocity contours of the axial section at $Re = 900$, $p = 40$ mm, and $l = 9$ mm are presented in Fig. 11 to analyze the effect of the slant angle. As shown in Fig. 11(a), cold fluid in the core flow region is guided towards the boundary region by the slant rod. When the slant angle is small ($\theta = 20°$), the disturbance in the boundary and fluid mixing are weak because the velocity components on the cross-sectional plane are small. This means that the intensity of the scour on the tube wall by the fluid and longitudinal vortex flow is not sufficiently strong. When the slant angle is large ($\theta = 40°$), although the velocity components on the cross-sectional plane increase, the amount of fluid guided towards the boundary by the slant rod is reduced, because most of the fluid passes the slant rod directly. Therefore, a moderate slant angle can be selected to achieve an optimum combination of the velocity components in the cross-sectional plane and the amount of fluid guided towards the boundary. It is clearly seen that the fluid mixing and boundary disturbance of a central slant rod with $\theta = 30°$ is stronger than that with $\theta = 40°$ and $\theta = 20°$. Similarly, the temperature contours of a central slant rod with $\theta = 30°$ is more uniform in the core flow region and its temperature gradient is larger in the boundary layer than those with $\theta = 40°$ and $\theta = 20°$, as shown in Fig. 11(b). Meanwhile, the results analyzed from the temperature and velocity contours of central slant rod with $\theta = 20°$ are better than that with $\theta = 40°$. Thus, the optimum slant angle is confirmed to be between 20 and 30°.

3.3. Effects of the rod pitch

Effects of the rod pitch on the average Nusselt number, friction factor and performance ratio $R3$ at $l = 9$ mm are shown in Figs. 12–14. Several general tendencies can be seen from Fig. 12. Firstly, the average Nusselt number increases with a decrease in rod pitch. Secondly, the distinctions of the average Nusselt number between

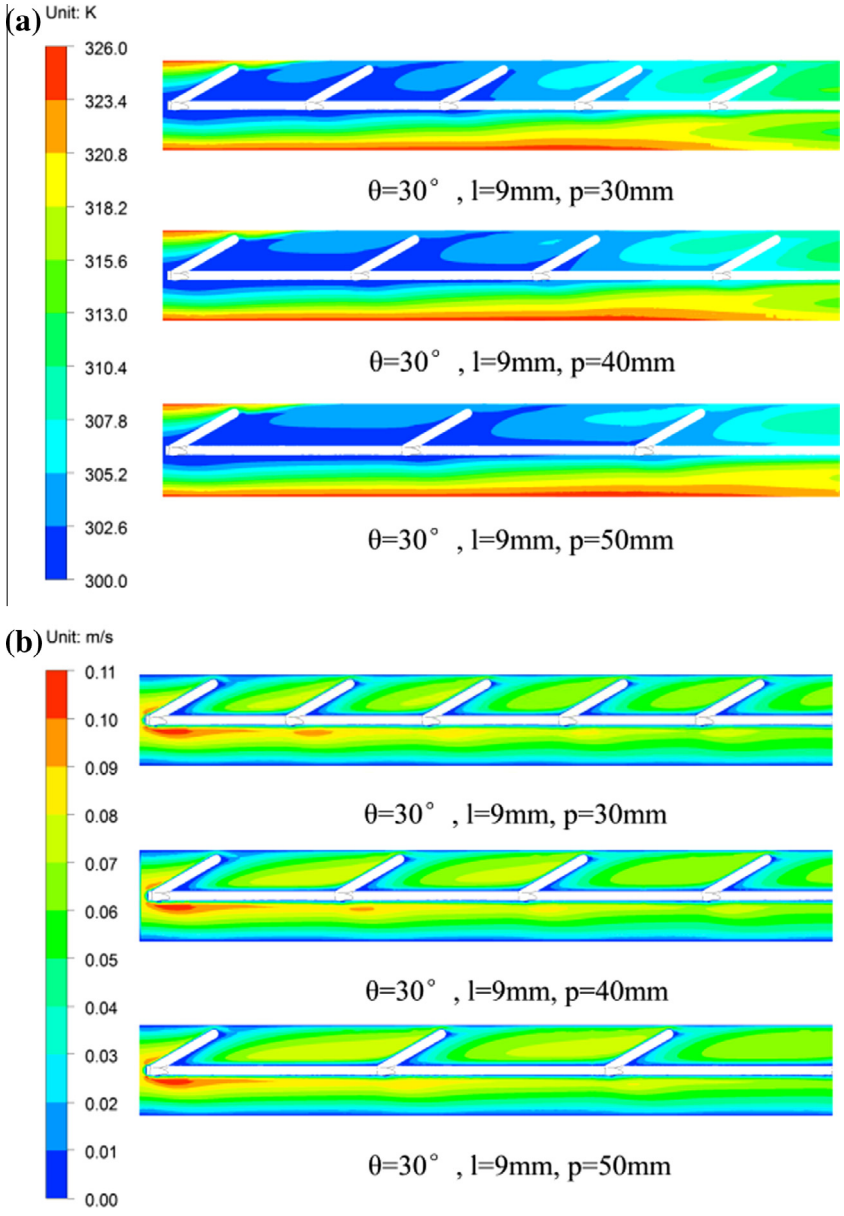

Fig. 15. Temperature contours (a) and velocity contours (b) at $Re = 900$, $\theta = 30°$, $l = 9$ mm.

different pitches increase as the slant angle increases. In other words, the larger the slant angle, the greater the effect of rod pitch on the average Nusselt number. From Fig. 13, it is found that the friction factor decreases with an increase in rod pitch and decreases with an increase in the Reynolds number for different slant angles. As Fig. 14 shows, the performance ratio $R3$ increases first and then decreases with the increase of Reynolds number. Under lower Reynolds number ($Re \leqslant 900$), the smaller rod pitch can obtain a higher the performance ratio $R3$ value, and the gap of the performance ratio $R3$ among different rod pitches is becoming larger when slant angle θ increases. Under higher Reynolds number, however, the gap of the performance ratio $R3$ among different rod pitches is limited. And the rod pitch of 50 mm obtains the largest performance ratio $R3$ when $\theta = 20°$, while the rod pitch of 40 mm obtains the largest performance ratio $R3$ when $\theta = 30°$. Therefore, we can conclude that there is an optimum rod pitch for overall thermal performance located between 30 mm and 50 mm. We tentatively put forward the interpretation as follows: when the rod pitch is small, the heat transfer is enhanced effectively, but the flow resistance is too large to obtain a desired overall thermal performance; when the rod pitch is large, although the flow resistance is lesser, the flow disturbance is too weak to achieve a high heat transfer performance. Therefore, there is a median of rod pitch for highest overall thermal performance.

Fig. 15 shows the effect of the rod pitch, the temperature and velocity contours of different rod pitches on an axial section at $Re = 900$, $\theta = 30°$ and $l = 9$ mm. It is seen that the disturbance of central slant rods on fluid is reinforced by the decrease in rod pitch. The temperature contours becomes more uniform in the core flow region and the boundary layer thins at a smaller rod pitch, as shown in Fig. 15(a). Therefore, the heat transfer is enhanced with a decrease in rod pitch, as shown in Fig. 12. Meanwhile, the intensification of the disturbance of the fluid results in increase of friction factor, as shown in Fig. 13. From Fig. 15(b), it is found that a single slant rod has a larger disturbance range in the direction of flow at a smaller slant angle. Thus, the effect of reducing the rod pitch on enhancing the heat transfer decreases with a decrease in slant angle, as shown in Fig. 12. However, the effects of pitch on friction factor at different slant angles are approximately equal, so when the slant angle is small, for example $\theta = 20°$, the larger

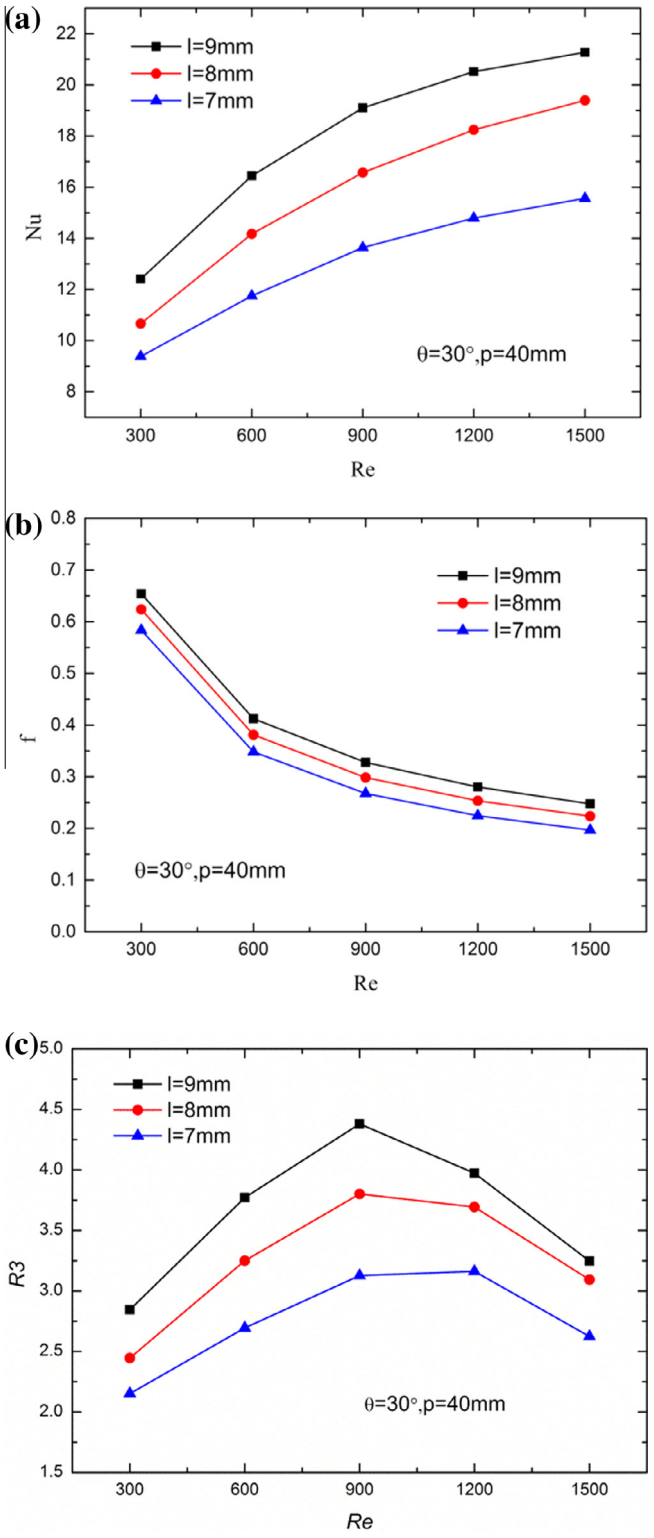

Fig. 16. Effects of the length of rod in the radial direction at $\theta = 30°$, $p = 40$ mm; (a) Nusselt number, (b) friction factor, (c) performance ratio $R3$.

rod pitch may gain a better thermal–hydraulic performance, as shown in Fig. 14.

3.4. Effects of the length of rod in the radial direction

Fig. 16 shows the effects of the rod length in the radial direction on the average Nusselt number, friction factor and performance ratio $R3$ at $\theta = 30°$, and $p = 40$ mm. An obvious trend is found whereby the average Nusselt number, friction factor and performance ratio $R3$ all increase with an increase in rod length in the radial direction. Fig. 17 presents the temperature and velocity contours of different rod lengths in the radial direction on axial section at $Re = 900$, $\theta = 30°$, and $p = 40$ mm. The slant rod approaches the tube wall with an increase in rod length in the radial direction, which means that the disturbance of slant rod on the fluid expands to the region near the tube wall as the rod length increases in the radial direction. Thus, the flow boundary layer becomes thinner at greater rod lengths in the radial direction, and its temperature contours become more uniform in the core flow region which leads to a larger temperature gradient in the boundary layer, as shown in Fig. 17. Therefore, the heat transfer is greatly enhanced when the rod length in the radial direction increases. Simultaneously, the enhancement of the disturbance on the fluid results in increase in the friction factor with increase in rod length in the radial direction.

3.5. Synergy angles

Guo et al. first proposed the field synergy theory in the past decade, which has been further developed by Tao et al. and Liu et al. [29–33]. According the field synergy theory, the thermal and hydraulic performances of the heat transfer process can be evaluated and analyzed by using synergy angles β and θ_1, which are defined as follows:

$$\beta = \arccos\frac{u \cdot \nabla T}{|u||\nabla T|} \tag{14}$$

$$\theta_1 = \arccos\frac{u \cdot \nabla P}{|u||\nabla P|} \tag{15}$$

The smaller the β (coordination between the velocity and temperature gradient fields), the higher the heat transfer rate (the larger Nu) is. Similarly, the smaller the θ_1 (coordination between the velocity and pressure gradient fields), the lower the flow resistance (the smaller f).

The synergy angles β and θ_1 at different parameters are presented in Figs. 18 and 19, respectively. It is clearly seen that the synergy angles β of all the tube with central slant rods are smaller than that of the plain tube. However, the synergy angles θ_1 are larger than that of the plain tube, which means that the heat transfer of the tube with central slant rods is effectively enhanced and the flow resistance is also increased. From the three green lines of different slant angles, it is found that the synergy angle β is the smallest when the slant angle $\theta = 30°$, followed by that of the centrally slant rod at $\theta = 20°$. At a slant angle $\theta = 40°$, the synergy angle β is the largest. However, the disparities of synergy angles θ_1 at different slant angles are limited. These are consistent with the trends of Nu and f shown in Figs. 8 and 9, respectively. Similarly, the three black lines show the effects of rod pitch on the thermal and hydraulic performances. It is clearly seen that the synergy angle β decreases with a decrease in rod pitch, but the synergy angle θ_1 increases with a decrease in rod pitch. This is in agreement with the tendencies of Nu and f shown in Figs. 12 and 13, respectively. The three lines with square points in various colors present the effects of rod length in the radial direction on the thermal and hydraulic performances. With an increase in rod length in the radial direction, the synergy angle β decreases and the synergy angle θ_1 increases. This is consistent with the trends of Nu and f shown in Fig. 16.

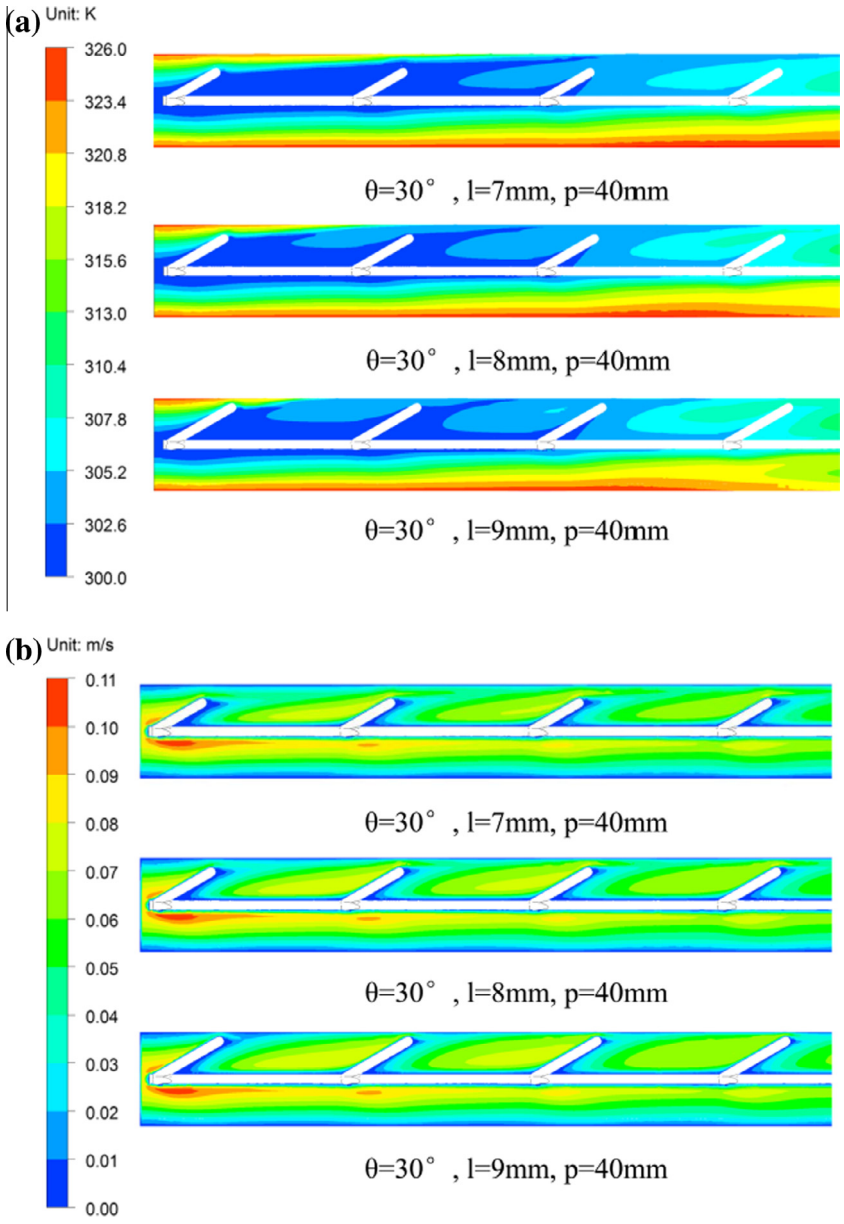

Fig. 17. Temperature contours (a) and velocity contours (b) at Re = 900, θ = 30°, p = 40 mm.

3.6. Correlations formula

First, a non-dimensional slant angle has been defined as follow: $S = \theta/\pi$. The empirical formulas are given as follows:

$$Nu = 2.345 \cdot Re^{0.343} \cdot \left(\frac{l}{R}\right)^{1.265} \cdot \left(\frac{p}{D}\right)^{-0.189} \cdot \left(1.015 - 35.885 \cdot \left(S - 0.167 \cdot \sqrt{\frac{l}{R}}\right)^2\right) \quad (16)$$

$$f = 43.707 \cdot Re^{-0.657} \cdot \left(\frac{l}{R}\right)^{0.775} \cdot \left(\frac{p}{D}\right)^{-0.472} \cdot S^{0.015} \quad (17)$$

As shown in Fig. 20, the maximum deviation of Nu between numerical simulation and the correlation formula is 20.3%, and most of the deviations are limited within ±10%. The deviations of f between numerical simulation and the correlation formula are controlled within ±10%.

3.7. Comparison with previous work

Comparisons of the heat transfer (Nu), friction factor (f) and overall thermal performance ($R3$) between the present work and previous work are shown in Fig. 21. Compared with small pipe inserts [18] and conical strip insert [34], although the heat transfer (Nu) of present work is lower, the friction factor is much lower than the previous work. Compared with the multiple regularly spaced twisted tapes [35] and widely used twisted tape [36],

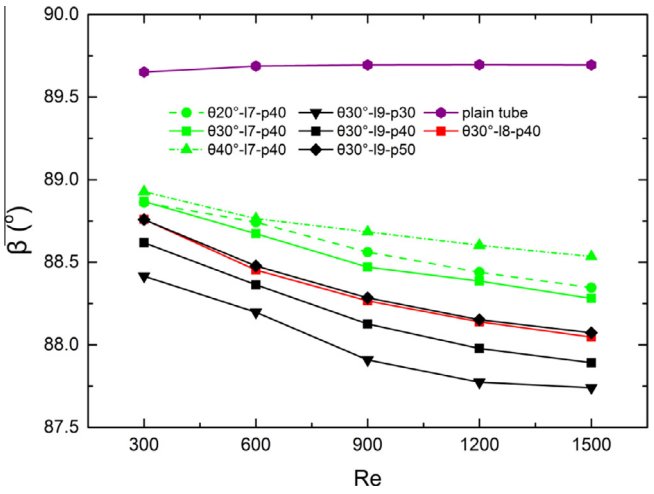

Fig. 18. The synergy angle (β) between the velocity and temperature gradient fields. (For interpretation of the references to color in this figure legend, the reader is referred to the web version of this article.)

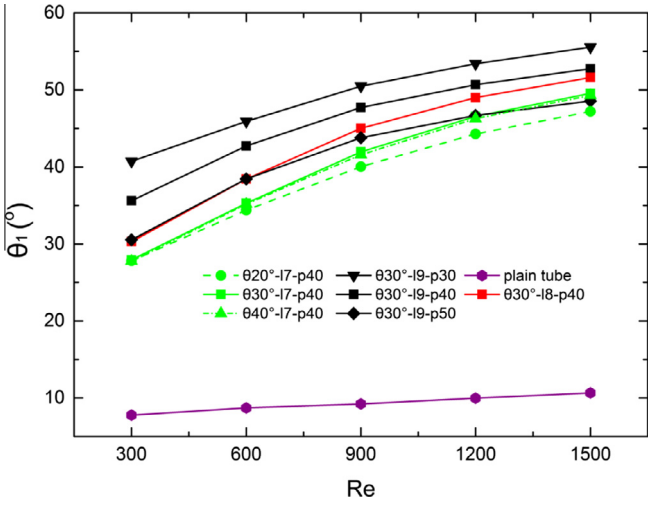

Fig. 19. The synergy angle (θ_1) between the velocity and pressure gradient fields. (For interpretation of the references to color in this figure legend, the reader is referred to the web version of this article.)

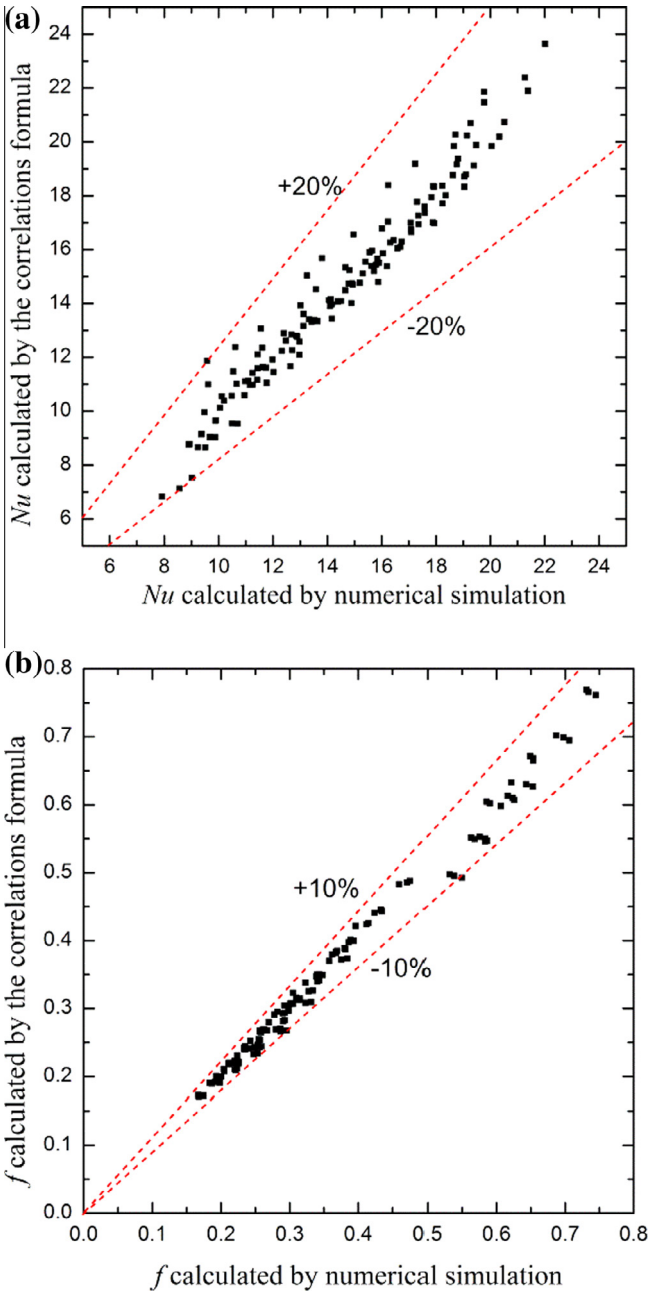

Fig. 20. Deviations of *Nu* and *f* calculated by the correlation formula and numerical simulation: (a) *Nu*. (b) *f*.

the present work is not only to enhance the heat transfer but also reduce the flow resistance. Therefore, the overall thermal performance of present work is slightly lower than the small pipe inserts and louvered strip insert but considerably higher than the multiple regularly spaced twisted tapes and twisted tape.

4. Conclusions

In the present study, characteristics of heat transfer and friction factor of laminar water flow in a circular tube fitted with central slant rod inserts is numerically studied and analyzed based on the physical quantity synergy principle. Results indicate that the flow structure of six longitudinal vortices in the core flow area of the tube is created. Such flow patterns are also found from SPIV (particle image velocimetry) measurement in the case where $\theta = 30°$, $p = 30$ mm, and $l = 9$ mm. The tube fitted with central slant rods obtains good heat transfer performance due to the enhanced fluid mixing achieved by the multi-vortices flow structure. The Nusselt number values are approximately 1.81–5.05 times that of the corresponding plain tube values, and the performance ratio *R*3 values are in the range of 1.74–4.60.

The effects of three parameters of the central slant rod were analyzed. The results are as follows:

(1) There is an optimum slant angle in the range of 20–30° for heat transfer performance, and the maximum slant angle increases with an increase in the rod length in the radial direction. However, the differences in friction factors between the different slant angles increase slightly with an increase in the rod length in the radial direction.
(2) Both the Nusselt number and the friction factor increase with a decrease in rod pitch. The Nusselt number is more sensitive to the rod pitch at larger slant angles.

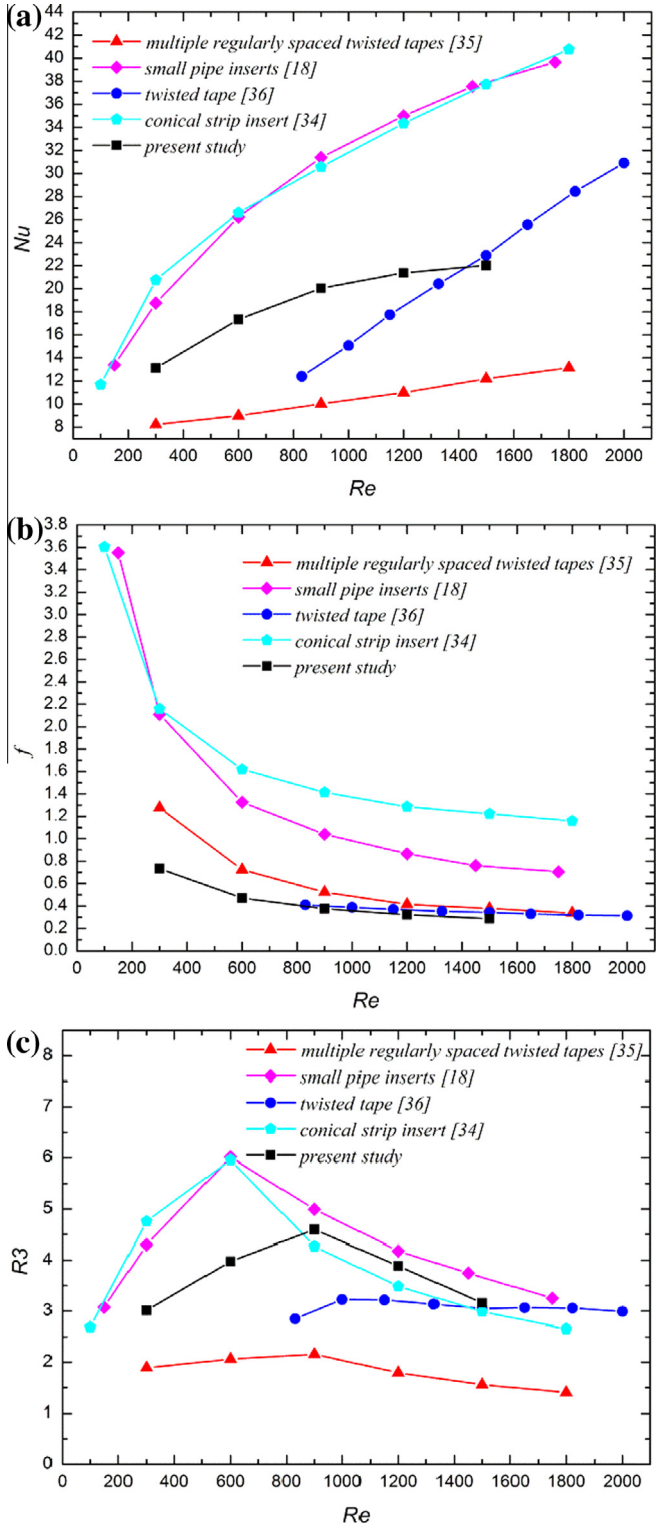

Fig. 21. Comparison with previous works: (a) *Nu*. (b) *f*. (c) *R*3.

(3) The Nusselt number and friction factor both increase with an increase in the rod length in the radial direction.

In summary, the optimum combination of geometric parameters of central slant angle for the best thermal–hydraulic performance is $\theta = 30°$, $p = 30$ mm, and $l = 9$ mm.

Acknowledgment

The work was supported by the National Key Basic Research Program of China (973 Program) (2013CB228302) and the National Natural Science Foundation of China (51376069).

References

[1] T.L.A.E. Bergles, R.M. Manglik, Current progress and new developments in enhanced heat and mass transfer, J. Enhanced Heat Transfer 20 (1) (2013) 1–15.
[2] R.M. Manglik, A.E. Bergles, Heat transfer and pressure drop correlations for twisted-tape inserts in isothermal tubes: Part I-laminar flows, J. Heat Transfer 115 (1993) 9.
[3] R.M. Manglik, A.E. Bergles, Heat transfer and pressure drop correlations for twisted-tape inserts in isothermal tubes: Part II-transition and turbulent flows, J. Heat Transfer 115 (1993) 7.
[4] S.K. Saha, A. Dutta, S.K. Dhal, Friction and heat transfer characteristics of laminar swirl flow through a circular tube fitted with regularly spaced twisted-tape elements, Int. J. Heat Mass Transfer 44 (22) (2001) 4211–4223.
[5] S. Jaisankar, T.K. Radhakrishnan, K.N. Sheeba, Experimental studies on heat transfer and friction factor characteristics of thermosyphon solar water heater system fitted with spacer at the trailing edge of twisted tapes, Appl. Therm. Eng. 29 (5–6) (2009) 1224–1231.
[6] S.R. Krishna, G. Pathipaka, P. Sivashanmugam, Heat transfer and pressure drop studies in a circular tube fitted with straight full twist, Exp. Therm. Fluid Sci. 33 (3) (2009) 431–438.
[7] S. Eiamsa-Ard, C. Thianpong, P. Eiamsa-Ard, P. Promvonge, Convective heat transfer in a circular tube with short-length twisted tape insert, Int. Commun. Heat Mass Transfer 36 (4) (2009) 365–371.
[8] S. Tarasevich, A. Yakovlev, A. Giniyatullin, A. Shishkin, Heat and mass transfer in tubes with various twisted tape inserts, in: ASME 2011 International Mechanical Engineering Congress and Exposition, American Society of Mechanical Engineers, 2011, pp. 697–702.
[9] S. Eiamsa-Ard, P. Promvonge, Performance assessment in a heat exchanger tube with alternate clockwise and counter-clockwise twisted-tape inserts, Int. J. Heat Mass Transfer 53 (7) (2010) 1364–1372.
[10] P. Murugesan, K. Mayilsamy, S. Suresh, P. Srinivasan, Heat transfer and pressure drop characteristics in a circular tube fitted with and without V-cut twisted tape insert, Int. Commun. Heat Mass Transfer 38 (3) (2011) 329–334.
[11] S.W. Chang, T.L. Yang, J.S. Liou, Heat transfer and pressure drop in tube with broken twisted tape insert, Exp. Therm. Fluid Sci. 32 (2) (2007) 489–501.
[12] D. Martínez, A. García, J. Solano, A. Viedma, Heat transfer enhancement of laminar and transitional Newtonian and non-Newtonian flows in tubes with wire coil inserts, Int. J. Heat Mass Transfer 76 (2014) 540–548.
[13] A. Fan, J. Deng, A. Nakayama, W. Liu, Parametric study on turbulent heat transfer and flow characteristics in a circular tube fitted with louvered strip inserts, Int. J. Heat Mass Transfer 55 (19) (2012) 5205–5213.
[14] P.B. Jasiński, Numerical study of the thermo-hydraulic characteristics in a circular tube with ball turbulators. Part 2: heat transfer, Int. J. Heat Mass Transfer 74 (2014) 473–483.
[15] X. Zhang, Z. Liu, W. Liu, Numerical studies on heat transfer and friction factor characteristics of a tube fitted with helical screw-tape without core-rod inserts, Int. J. Heat Mass Transfer 60 (2013) 490–498.
[16] P.W. Deshmukh, R.P. Vedula, Heat transfer and friction factor characteristics of turbulent flow through a circular tube fitted with vortex generator inserts, Int. J. Heat Mass Transfer 79 (2014) 551–560.
[17] C. Zhang, D. Wang, Y. Zhu, Y. Han, J. Wu, X. Peng, Numerical study on heat transfer and flow characteristics of a tube fitted with double spiral spring, Int. J. Therm. Sci. 94 (2015) 18–27.
[18] W. Tu, Y. Tang, J. Hu, Q. Wang, L. Lu, Heat transfer and friction characteristics of laminar flow through a circular tube with small pipe inserts, Int. J. Therm. Sci. 96 (2015) 94–101.
[19] W. Tu, Y. Tang, B. Zhou, L. Lu, Experimental studies on heat transfer and friction factor characteristics of turbulent flow through a circular tube with small pipe inserts, Int. Commun. Heat Mass Transfer 56 (2014) 1–7.
[20] A. Bejan, A.D. Kraus, Heat Transfer Handbook, John Wiley & Sons, 2003.
[21] K. Yang, W. Liu, Forming an equivalent thermal boundary layer for fully-developed laminar tube flow and its field synergy analysis, J. Eng. Thermophys. 28 (2) (2007) 283.
[22] W. Liu, K. Yang, Mechanism and numerical analysis of heat transfer enhancement in the core flow along a tube, Sci. China Ser. E Technol. Sci. 51 (8) (2008) 1195–1202.
[23] W. Liu, Z. Liu, H. Jia, A. Fan, A. Nakayama, Entransy expression of the second law of thermodynamics and its application to optimization in heat transfer process, Int. J. Heat Mass Transfer 54 (13) (2011) 3049–3059.
[24] H. Jia, W. Liu, Z. Liu, Enhancing convective heat transfer based on minimum power consumption principle, Chem. Eng. Sci. 69 (1) (2012) 225–230.
[25] J. Wang, Z. Liu, F. Yuan, W. Liu, G. Chen, Convective heat transfer optimization in a circular tube based on local exergy destruction minimization, Int. J. Heat Mass Transfer 90 (2015) 49–57.
[26] J. Wang, W. Liu, Z. Liu, The application of exergy destruction minimization in convective heat transfer optimization, Appl. Therm. Eng. (2014).

[27] W. Liu, H. Jia, Z. Liu, H. Fang, K. Yang, The approach of minimum heat consumption and its applications in convective heat transfer optimization, Int. J. Heat Mass Transfer 57 (1) (2013) 389–396.
[28] R.M. Manglik, A.E. Bergles, Swirl flow heat transfer and pressure drop with twisted-tape inserts, Adv. Heat Transfer 36 (2003) 183–266.
[29] Z. Guo, D. Li, B. Wang, A novel concept for convective heat transfer enhancement, Int. J. Heat Mass Transfer 41 (14) (1998) 2221–2225.
[30] Z.-Y. Guo, W.-Q. Tao, R. Shah, The field synergy (coordination) principle and its applications in enhancing single phase convective heat transfer, Int. J. Heat Mass Transfer 48 (9) (2005) 1797–1807.
[31] W. Liu, Z. Liu, Z. Guo, Physical quantity synergy in laminar flow field of convective heat transfer and analysis of heat transfer enhancement, Chin. Sci. Bull. 54 (19) (2009) 3579–3586.
[32] W. Liu, Z. Liu, S. Huang, Physical quantity synergy in the field of turbulent heat transfer and its analysis for heat transfer enhancement, Chin. Sci. Bull. 55 (23) (2010) 2589–2597.
[33] L. Wei, L. Zhichun, M. Tingzhen, G. Zengyuan, Physical quantity synergy in laminar flow field and its application in heat transfer enhancement, Int. J. Heat Mass Transfer 52 (19) (2009) 4669–4672.
[34] Y. You, A. Fan, W. Liu, S. Huang, Thermo-hydraulic characteristics of laminar flow in an enhanced tube with conical strip inserts, Int. J. Therm. Sci. 61 (2012) 28–37.
[35] X. Zhang, Z. Liu, W. Liu, Numerical studies on heat transfer and flow characteristics for laminar flow in a tube with multiple regularly spaced twisted tapes, Int. J. Therm. Sci. 58 (2012) 157–167.
[36] K. Wongcharee, S. Eiamsa-Ard, Friction and heat transfer characteristics of laminar swirl flow through the round tubes inserted with alternate clockwise and counter-clockwise twisted-tapes, Int. Commun. Heat Mass Transfer 38 (3) (2011) 348–352.